Am J Cancer Res 2022;12(11):5255-5270
www.ajcr.us /ISSN:2156-6976/ajcr0145501

Original Article

In vivo growth of subclones derived from Lewis lung carcinoma is determined by the tumor microenvironment

Ben-Ling Xu[1], Xiao-Ming Wang[2], Guang-Yu Chen[1], Peng Yuan[3], Lu Han[1], Peng Qin[1], Tie-Peng Li[1], Hong-Qin You[1], Cheng-Juan Zhang[4], Xiao-Min Fu[1], Long Yuan[2*], Zi-Bing Wang[1*], Quan-Li Gao[1*]

Departments of [1]Immunotherapy, [2]General Surgery, [3]Breast Surgery, The Affiliated Cancer Hospital of Zhengzhou University & Henan Cancer Hospital, Zhengzhou 450008, Henan, P. R. China; [4]Center of Bio Repository, The Affiliated Cancer Hospital of Zhengzhou University & Henan Cancer Hospital, Zhengzhou 450008, Henan, P. R. China. [*]Equal contributors.

Received July 22, 2022; Accepted November 2, 2022; Epub November 15, 2022; Published November 30, 2022

Abstract: Heterogeneity is a fundamental feature of human tumors and plays a major role in drug resistance and disease progression. In the present study, we selected single-cell-derived cell lines (SCDCLs) derived from Lewis lung carcinoma (LLC1) cells to investigate tumorigenesis and heterogeneity. SCDCLs were generated using limiting dilution. Five SCDCLs were subcutaneously injected into wild-type C57BL/6N mice; however, they displayed significant differences in tumor growth. Subclone SCC1 grew the fastest in vivo, whereas it grew slower in vitro. The growth pattern of SCC2 was the opposite to that of SCC1. Genetic differences in these two subclones showed marked differences in cell adhesion and proliferation. Pathway enrichment results indicate that signal transduction and immune system responses were the most significantly altered functional categories in SCC2 cells compared to those in SCC1 cells in vitro. The number and activation of $CD3^+$ and $CD8^+$ T cells and NK cells in the tumor tissue of tumor-bearing mice inoculated with SCC2 were significantly higher, whereas those of myeloid cells were significantly lower, than those in the SCC1 and LLC1 groups. Our results suggest that the in vivo growth of two subclones derived from LLC1 was determined by the tumor microenvironment rather than their intrinsic proliferative cell characteristics.

Keywords: Cancer cell line, heterogeneity, Lewis lung carcinoma, immunological characterization, single cell-derived cell lines

Introduction

Lung cancer is the second most commonly diagnosed cancer and the leading cause of cancer-related deaths worldwide [1-3]. Heterogeneity is a fundamental feature of human tumors and plays a major role in drug resistance and disease progression [4]. Molecular analyses of lung cancers of the same lineage and histology, such as EGFR mutation status and PD-L1 expression, reveal such heterogeneity and can affect care decisions [5-8]. To study human cancer biology, researchers use patient biopsies, tissue from the surgical resection of tumors, or genetically engineered mouse models; however, in the laboratory, lung cancer is often modeled using established cell lines [9-11].

Lewis lung carcinoma (LLC1) is a commonly used lung cancer cell line that represents an important example of lung cancer cells that have facilitated fundamental discoveries in cancer biology and translational medicine [12-16]. LLC1 cells form multilayers in flasks without becoming confluent. Cell lines are often regarded as clonal and genetically stable; however, findings are often difficult to reproduce, leading investigators to conclude that the findings were either weak or that the studies were not carefully conducted. Research reproducibility can be compromised by both biological and technical variation. The complexity inherent to biological systems poses a major challenge.

Several recent studies have highlighted the heterogeneity of cancer cell lines across laborato-

ries [17-19]. However, little is known about how such genomic variability affects the cellular phenotypes of different LLC1 single-cell derivatives and how these, in turn, affect biological research outcomes.

To better understand the heterogeneous nature of LLC1, in the present study, we evaluated the morphology, receptor status, drug sensitivity, tumor growth, and tumor-infiltrating lymphocyte differences to profile the genetic and immunological characterization of LLC1 and its single-cell derivatives.

Materials and methods

Ethics statement

The investigation has been performed in accordance with the ethical standards of the Declaration of Helsinki and the national and international guidelines, and has been approved by the Life Science Ethics Review Committee of Zhengzhou University (Project # 82172700, Supplementary File 1).

Cell line and generation of single-cell clones

To investigate whether subpopulations within LLC1 have different biological behaviors, we sought to systematically characterize the intrinsic growth dynamics of individuals in vitro and in vivo by isolating single-cell clonal populations from LLC1. LL/2 (LLC1) (ATCC® CRL-1642™) tumor cells were purchased from the American Type Culture Collection (ATCC, Manassas, USA). LLC1 and its clonal derivatives were used and cultured according to the ATCC guidelines. Briefly, cells were thawed from frozen stocks and expanded using Dulbecco's modified Eagle's medium-based growth medium containing 10% heat-inactivated fetal bovine serum and 1% penicillin-streptomycin-glutamine (Life Technologies). Cells were incubated at 37°C with 5% CO_2 and passaged twice a week using trypsin-EDTA (0.25%) (Life Technologies).

Clones were developed using limiting dilution, and LLC1 cells were placed in 96-well plates at a density of 1 cell/well. Each well was visualized under a light microscope 4 h later, and wells with more than one cell were discarded. After sufficient growth, the colonies were transferred to vessels of increasing size to expand the cell population and were subjected to low-passage primary culture to establish single-cell-derived cell lines (SCDCLs). The cloned subpopulations obtained after 4-5 passages (7-13 days of culture after cloning) were divided into multiple samples; some were frozen until needed for subsequent experiments. The number of passages was controlled. All SCDCLs were cultured under the same conditions and passaged at least five but no more than eight times. All cells were confirmed to be mycoplasma-free using the MycoAlert Mycoplasma Detection Kit (Lonza), according to the manufacturer's instructions.

Photography of LLC1 and SCDCLs

Plates were imaged with Leica DMIL LED microscopes using LAS Version 4.5.0 software. Images of each well were captured at 100 × magnification.

Doubling time

Doubling time was calculated by dividing the duration of the experiment (120 h) by the number of generations. Each cell population was placed into a 6-well plate (Corning) at a density of 7×10^3 cells/well. Cells were harvested by trypsinization on days 1, 3, and 5, and counted manually. Each experiment was performed in triplicate and repeated three times. Doubling time was calculated using http://www.doublingtime.com/compute.php. The cell doubling time differences between the whole-process replicates were less than 2 h.

Drug sensitivity assay and PD-L1 expression

Drug sensitivity analysis via MTT assay was performed at the same time for cells from LLC1 and two SCDCLs, SCC1 and SCC2. The three cell lines, after recovery from liquid nitrogen, were collected after 1-2 passages, grown in log phase, and treated with either vehicle only or with the indicated cytotoxic drug (cisplatinum, paclitaxel, and albumin paclitaxel) to a final concentration in the range of 0-500 μM for 24 h before harvest. PD-L1 expression was analyzed using fluorescence activated cell sorting (FACS) before and after cytotoxic drug treatment at the indicated concentrations. 7AAD viability staining (Biolegend) was used to assess the viability of the cells. Tumor cells (1×10^6) were mixed with 5 μL of PD-L1-APC-specific

antibodies (Biolegend) and was incubated on ice for 20 min in the dark. After incubation, the samples were washed with FACS buffer (5% BSA in PBS, 0.09% sodium azide). The pellets were suspended in 300 μL of FACS buffer and acquired on a BD FACS Conto II flow cytometer. Subsequetly, the data was analyzed using the FlowJo software (TreeStar Inc.).

Whole-exome sequencing and mutation calling

Genomic DNA was extracted from LLC1, SCC1, and SCC2 cells using CTAB. OE Biotech (Shanghai, China) provided exome capture, high-throughput sequencing, and common filtering. Clustering of the index-coded samples was performed on a cBot Cluster Generation System using an Illumina PE Cluster Kit (Illumina, USA) according to the manufacturer's instructions. After cluster generation, DNA libraries were sequenced on an Illumina HiSeq2000 platform and 150 bp paired-end reads generated.

The raw data were compiled in fastp format. Mapping and variant analysis reads were mapped to the mouse genome (GRCm38.p6) using BWA (0.7.17) with default parameters. The mapped reads were sorted and indexed using SAM tools (version 1.9). GATK4 (version 4.1.9.0) was used for recalibration of the base quality score and for single nucleotide polymorphism (SNP) and insertion/deletion (INDEL) realignment.

RNA extraction, library preparation, and mRNA sequencing

Total RNA was extracted using the mirVana miRNA Isolation Kit (Ambion), following the manufacturer's protocol. RNA integrity was evaluated using the Agilent 2100 Bioanalyzer (Agilent Technologies, Santa Clara, CA, USA). Samples with an RNA integrity number ≥ 7 were subjected to subsequent analysis. Libraries were constructed using the TruSeq Stranded mRNA LTSample Prep Kit (Illumina, San Diego, CA, USA) according to the manufacturer's instructions. These libraries were then sequenced on an Illumina HiSeq X Ten platform and 150 bp paired-end reads were generated.

Transcriptome sequencing and analysis were conducted by OE Biotech (Shanghai, China). Raw data were processed using Trimmomatic software. Reads containing poly-N and low-quality reads were removed to obtain clean reads. The clean reads were then mapped to the reference genome using hisat2. The FPKM value of each gene was calculated using cufflinks, and the read counts of each gene were obtained by HTSeq-count. Differentially expressed genes (DEGs) were identified using the DESeq (2012) R package to estimate the size factors. A p-value < 0.05 and a fold-change > 2 or < 0.5 were set as the thresholds for significant differential expression. Hierarchical cluster analysis of DEGs was performed to explore gene expression patterns. GO enrichment and KEGG pathway enrichment analyses of DEGs were performed using the software R based on a hypergeometric distribution.

Real-time PCR assay

Total RNA from LLC1, SCC1, and SCC2 cells was isolated, and cDNA was synthesized using TransScript All-in-One First-Strand cDNA Synthesis SuperMIX for qPCR. Real-time PCR was performed using the Perfect StartTM Green qPCR SuperMix. Reaction mixtures were prepared according to the manufacturer's protocol. The relative mRNA levels of target genes were normalized to that of the β-actin. Detailed information about the primers used is provided in Supplementary Table 1.

Mice

Wild-type C57BL/6N mice were purchased from Beijing Vital River Laboratory Animal Technology (Beijing, China) and were randomly allocated to each group. All experiments were conducted at the China-US (Henan) Hormel Cancer Institute and complied with the National Research Council Guide for the Care and Use of Laboratory Animals. Female mice aged 6-8 weeks were used and maintained in a specific pathogen-free facility according to the guidelines for experimental animals at the China-US (Henan) Hormel Cancer Institute. Food and water were provided ad libitum.

Tumor inoculation

Mice were inoculated with 1×10^6 cells of LLC1 and its SCDCLs in 100 μL of phosphate-buffered saline, via subcutaneous injection into the right flank. Tumor growth was monitored every 2-3 d. Tumor width and length were measured using calipers, and tumor volume was calculat-

ed as L × W^2/2. Mice with a tumor volume ≥ 2 cm^3 or a tumor site that became inflamed or ulcerated were euthanized.

Immune profiling studies

Eighteen days post-tumor inoculation, mice were euthanized, and tumors and lungs were collected. Tumors were cut into small pieces, digested at 37°C for 1 h in Roswell Park Memorial Institute medium with collagenase IV (1 mg/mL) and DNase (10 μg/mL) (both from Sigma), and then tumor-infiltrating lymphocytes (TILs) were isolated by centrifugation on a discontinuous Percoll gradient (GE Healthcare).

Following cell isolation and preparation, samples were stained for FACS using surface antibodies (20 min each at 4°C) as shown in Supplementary Table 2. Samples were run on a BD FACS Celesta and analyzed using FlowJo software. TILs were surface-stained with antibodies and 7-AAD (BioLegend) following the manufacturer's instructions. The transcription factors (TFs) validated in vitro were further validated in the tumor tissues using quantitative RT-PCR.

Anti PD-1 treatment

Wild-type C57BL/6N mice were treated intraperitoneally with 200 μg of either anti-PD-1 (murine IgG2a, clone 29F.1A12, BioXCell) or their respective isotype control (IgG2a, clone C1.18.4, BioXCell) on days 8, 11, and 14 post-tumor inoculation for the LLC1 and SCC1 groups, and on days 15, 18, and 21 post-tumor inoculation for the SCC2 group (tumor size 50-100 mm^3). Mice were sacrificed 18 or 25 d after the injection of tumor cells (n = 5 per group), and at least two independent experiments were performed.

Histology and lung metastases tumor burden scoring

For the analysis of pulmonary metastasis, mice were sacrificed 18 d after the subcutaneous injection of tumor cells. The lungs were removed, fixed in paraformaldehyde, and a 3-μm thick section was removed every 200 μm throughout the lung. Sections were stained with hematoxylin and eosin and screened histologically.

For histological quantification, tissue slides were examined by a pathologist blinded to experimental treatment. Images of tissue sections were captured at 10 × magnification.

Statistical analysis

Graphs and statistical analyses were performed using Prism 8.0.2. (GraphPad Software). Depending on the experimental setup, unpaired Student's t-test (two-tailed), a one-way ANOVA (Dunnett's multiple comparison test), or a two-way ANOVA was used to assess significance. The exact significance values are shown in all graphs, and the number of biological or technical replicates (n) is given in Figure legends. Significance levels are defined as ns (not significant, $P > 0.05$), *$P < 0.05$, **$P < 0.01$, ***$P < 0.001$, and ****$P < 0.0001$.

Results

Isolation and morphology heterogeneity of SCDCLs from LLC1

Using limiting dilution, we established 43 SCDCLs from LLC1. The flowchart in Supplementary Figure 1A summarizes the analytical procedure used.

SCDCLs exhibited distinct growth patterns and kinetics. We chose five clones (SCC1, SCC2, SCC3, SCC4, and SCC5) for subsequent experiments based on their variable morphology in culture and time to reach confluence (range: 10-14 d).

The five clonal cell lines exhibited distinctive morphological traits. SCC1 and SCC2 cells were flat, elongated, and adhered better to plastic than any of the other clones, whereas SCC1 cells tended to form a cord and SCC2 cells were almost homogeneous. SCC3 and SCC4 had mixed morphology, with rounded or flat elongated cells, and tended to associate in multicellular agglomerates, forming cord or clone balls, and adhered better to plastic than SCC5, which was small, rounded, tended to form clone balls, and adhered more poorly than any of the other clones (Supplementary Figure 1B).

Growth heterogeneity of SCDCLs

To better understand the heterogeneity among the SCDCL strains, we analyzed their doubling times. The doubling time was 13.44 ± 0.22 h for LLC1, which was significantly lower than those for clones SCC1 (14.99 ± 0.16 h, $P = 0.0005$), SCC3 (18.83 ± 0.32 h, $P < 0.0001$),

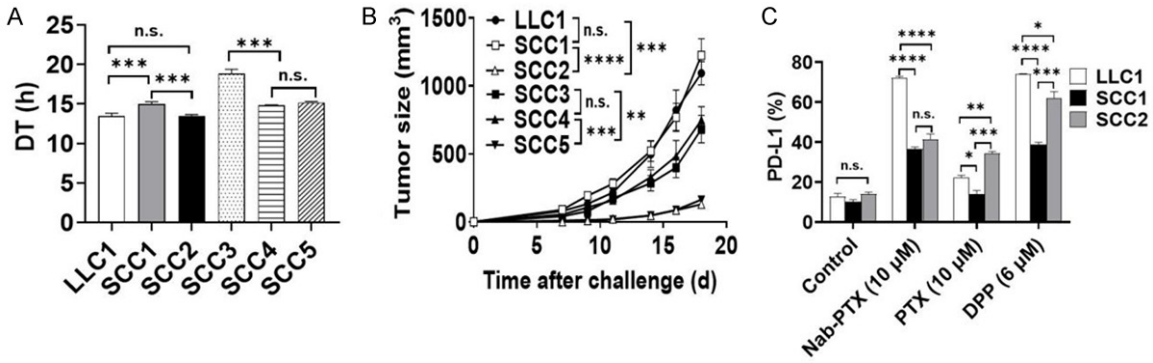

Figure 1. Clonal populations derived from the LLC1 cell line vary in population doubling time and dose response to cytotoxic drugs. A. Doubling time of LLC1 and clonal cell lines (SCDCLs) grown for 5 d. Doubling time was calculated using http://www.doublingtime.com/compute.php. Data shown as mean ± SEM from three independent experiments; *p*-values from one-way ANOVA, corrected for multiple comparisons using Dunnett's method. B. In vivo tumor growth in C57BL/6N mice inoculated with the LLC1 cell line and five SCDCLs (n = 5). Data are mean ± SEM. *p*-values from two-way ANOVA. C. Expression of PD-L1 in SCDCLs after cytotoxic drug treatment. Each experiment was performed in triplicate and repeated three times. *p*-values from one-way ANOVA. *P < 0.05, **P < 0.01, ***P < 0.001, ****P < 0.0001.

SCC4 (14.8 ± 0.04 h, P = 0.0017), and SCC5 (15.19 ± 0.06 h, P = 0.0002), but did not differ from clone SCC2 (13.51 ± 0.08 h). Doubling time for clone SCC2 was significantly lower than those for clones SCC1 (P = 0.0008), SCC3 (P < 0.0001), SCC4 (P = 0.0026), and SCC5 (P = 0.0003). The doubling time of clone SCC3 was significantly higher than that of clone SCC4 (P < 0.0001). Each experiment was performed in triplicate and repeated three times (**Figure 1A**).

To assess tumor cell growth characteristics in vivo, LLC1 and the five SCDCLs were injected into mice. All of the cell lines were tumorigenic, but each displayed significant differences in tumor growth. LLC1 and SCC1 tumors developed the fastest. Multiple tumors from these cell lines were palpable by day 5 and reached volumes > 100 mm^3 by day 8 (compared to day 9 for SCC4, day 10 for SCC3, and day 16 for SCC2 and SCC5).

The tumors in the SCC1 group grew significantly faster than those in the SCC2 (P < 0.0001), SCC3 (P = 0.0111), SCC4 (P = 0.0236) and SCC5 group (P < 0.0001), whereas there was no difference between the SCC1 and LLC1 group (P = 0.6612). The tumors in the SCC2 group grew significantly slower than those in the LLC1 (P = 0.0002), SCC3 (P = 0.0009), and SCC4 group (P = 0.0003), whereas there was no difference between the SCC2 and SCC5 group (P = 0.5330). The tumors in the SCC3 group grew significantly slower than those in the LLC1 group (P = 0.0359), grew significantly faster than those in the SCC5 group (P = 0.0010), whereas there was no significant difference between the SCC3 and SCC4 group (P = 0.5614). The tumors in the SCC4 group grew significantly faster than those in the SCC5 group (P = 0.0003), whereas there was no significant difference between the SCC4 and LLC1 group (P = 0.0738). The tumors in the SCC5 group grew significantly slower than those in the LLC1 group (P = 0.0002). Tumor growth rates revealed differences in SCDCL growth rates between in vitro and in vivo environments. SCC1 grew fastest in vivo and slower in vitro, whereas SCC2 showed the opposite pattern, growing slowest in vivo and faster in vitro (**Figure 1B**). These two clones were, thus, selected for subsequent study.

SCDCLs respond differently to cytotoxic drugs

We next tested the hypothesis that SCDCLs respond differently to cytotoxic drugs. Drug sensitivity results are presented in **Table 1**. Treatment with cisplatin (DDP) revealed significant differences between LLC1 cells (IC50 (half maximal inhibitory concentration) 7.9 μM) and SCC2 cells (IC50 12.5 μM, P < 0.0001), but no difference between LLC1 and SCC1 cells (IC50 7.8 μM, P = 0.9297). Similar effects on paclitaxel (PTX) sensitivity were observed in the SCDCLs. For albumin paclitaxel (Nab-PTX), the IC50 value of SCC1 cells (27.7 μM) was significantly lower than that of SCC2 cells (915.7 μM,

Table 1. Drug sensitivity of LLC1, SCC1, and SCC2 (μM)

	LLC1		SCC1		SCC2	
	IC50	95% CI	IC50	95% CI	IC50	95% CI
DDP	7.9	7.5-8.3	7.8	7.6-8.1	12.5	11.9-13.1
PTX	5.9	2.2-12.6	17.6	7.1-35.0	56.8	31.4-69.0
Nab-PTX	282.2	172.7-545.9	27.7	18.5-41.3	915.7	479.3-2739

DDP: cisplatin; PTX: paclitaxel; Nab-PTX: albumin paclitaxel.

P < 0.0001), whereas there was no significant difference between the SCC1 and LLC1 cells (27.7 μM vs. 282.2 μM, P = 0.0648). IC50 curve was shown as a Supplementary Figure 2. The IC50 of DDP and PTX to LLC1 and SCC1 cells was much lower than that of SCC2 cells, whereas the IC50 of DDP to LLC1 cells was similar to that of SCC1 cells, indicating that SCC2 cells have greater resistance to DDP than LLC1 and SCC1 cells. All the cell lines appeared more sensitive to DDP and PTX than to Nab-PTX because of their lower concentration. The parental LLC1 cell population, the most resistant to Nab-PTX, was the most sensitive to PTX. SCC1 cells were most resistant to Nab-PTX and most sensitive to DDP, SCC2 cells had similar responses. Notably, the SCC1 and SCC2 cells identified in this study exhibited different sensitivities to anticancer drugs.

Moreover, the expression of PD-L1 was upregulated after cytotoxic drug treatment. The expression of PD-L1 increased to 74% in LLC1 cells after DDP treatment (6 μM), significantly more than those in SCC1 (38.9%, P < 0.0001) and SCC2 (61.9%, P = 0.0138) cells. Similar effects on Nab-PTX (10 μM) treatment in LLC1 and SCDCLs were found. However, the expression of PD-L1 in LLC1 (22.2%, P = 0.0018) and SCC1 (14%, P = 0.0001) cells was significantly lower than that in SCC2 cells (34.4%) after PTX treatment (**Figure 1C**).

Hence, we used comprehensive genome and transcriptome profiling to elucidate the different responses of SCDCLs to drug sensitivity and tumor growth.

Whole exome sequencing of SCDCLs reveals genetic variants

The differences observed in vitro and in vivo prompted us to further explore the genetic variation across LLC1, SCC1, and SCC2 cells using whole exome sequencing (WES). Based on SNP annotation, we compared these three groups and identified 230 genetic variants that were observed only in the SCC2 group (**Figure 2A**), 208 that were observed only in the LLC1 group, and 114 that were observed only in the SCC1 group. Based on INDEL alignment, we identified 172, 153, and 102 genetic variants observed only in the SCC2, LLC1, and SCC1 groups, respectively. **Figure 2B** shows the number of different mutation types in the LLC1, SCC1, and SCC2 cells. Somatic mutation rates varied among the samples. We further analyzed the mutational spectra of these cells. Among all mutations, C > A transversions and C > T and T > C transitions were the predominant changes in LLC1, C > A and C > G transversions increased dramatically in SCC2 cells, whereas the proportion of T > C transitions decreased in SCC2 cells (**Figure 2C**). These findings highlight that SCC1 and SCC2 cells derived from the same parental population differed in their mutational landscapes. WES showed EGFR (p.P992P) and KRAS (p.G12C) mutations in the parental cell population and in these two SCDCLs. The number of somatic SNVs and the distribution of different mutation types are shown in **Figure 2D**. A circos plot of all detected mutations comparing LLC1 to SCC2 cells is shown in **Figure 2E**.

Gene expression variation in SCDCLs

We subsequently analyzed gene expression profiles of LLC1, SCC1, and SCC2 cells via transcriptome sequencing. Principal component analysis (PCA) on global gene expression profiles separated SCC1 and SCC2 populations (Supplementary Figure 3A). The three strains also showed extensive expression variation: 959-1333 genes were differentially expressed by at least a fold-change > 2 or fold-change < 0.5 between pairs of strains (P < 0.05). In addition, DEGs converged on important biological pathways. In SCC2, 635 genes were upregulated and 698 genes were downregulated compared to that in SCC1; and 187 genes were upregulated and 772 genes were downregulated in SCC2 compared to that in LLC1 (**Figure 3A**), with similar findings for SCC1 versus LLC1. LLC1 and SCC2 cells had 136 unique DEGs (**Figure 3B**). Components of the membrane,

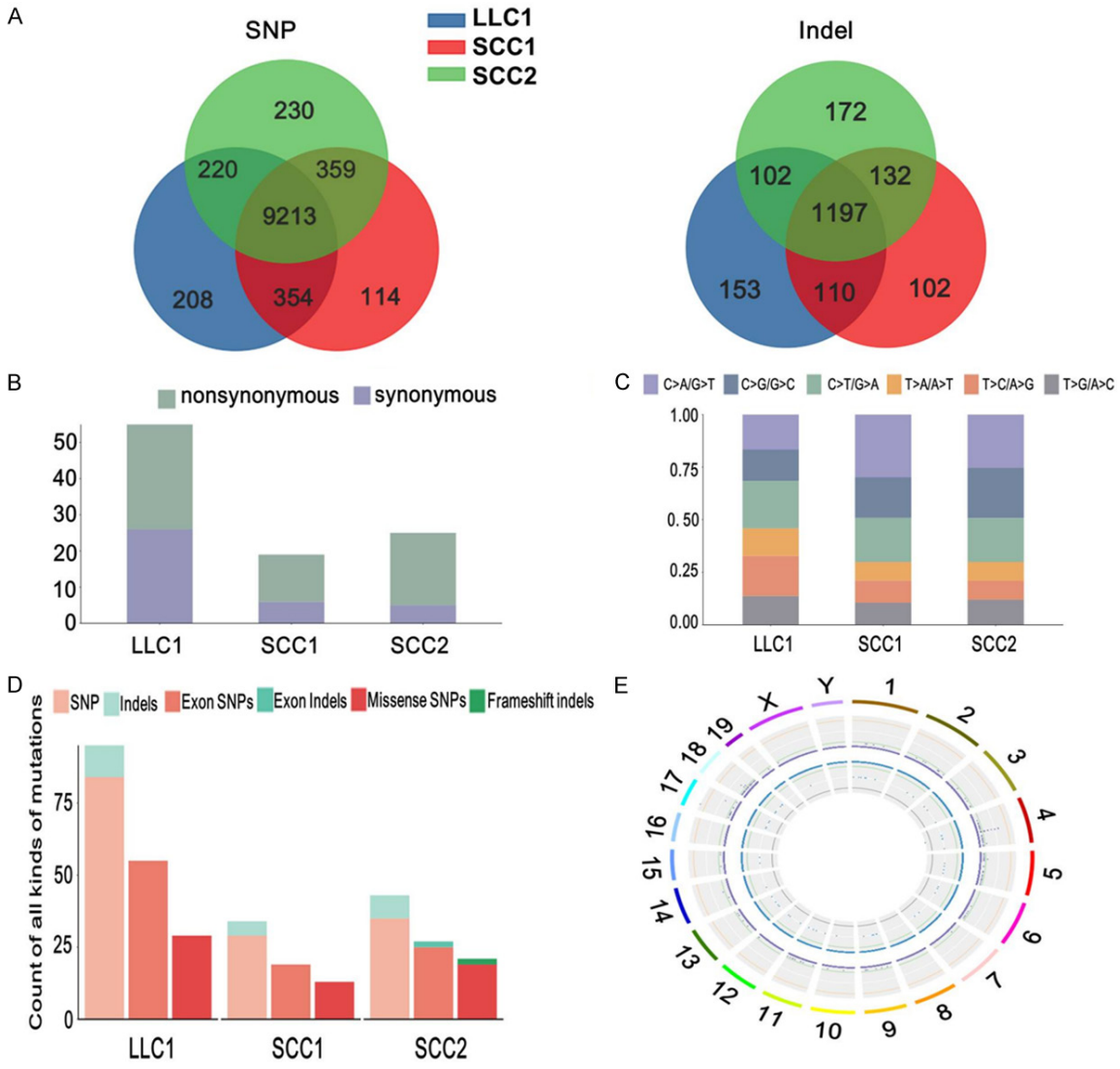

Figure 2. WES analysis of LLC1, SCC1, and SCC2 cells. A. Venn diagram of unique and shared genetic variants. B. Number of somatic SNVs and the distribution of different mutation types. C. Mutation spectrum of LLC1 and the single-cell clonal lines SCC1 and SCC2. Color codes represent the fraction of different base substitutions. D. Number of somatic SNVs and the distribution of different mutation types. E. Circos plot of all detected mutations comparing LLC1 to SCC2 cells.

plasma membrane, and cell adhesion ranked in the top 30 GO terms in SCC2 compared to that in SCC1 cells (**Figure 3C**). To determine the functional space of these DEGs, we conducted pathway enrichment analyses using KEGG pathway classification. Significant enrichment occurred in genes involved in signal transduction and the immune system when comparing SCC2 to SCC1 cells; 188 DEGs converged on signal transduction pathways and 105 DEGs converged on immune system pathways (**Figure 3D**). Similar results were observed when comparing SCC2 and LLC1 cells (Supplementary Figure 4A and 4B). Components of the membrane, plasma membrane, and cell adhesion were also ranked in the top 30 GO terms in SCC1 cells compared to LLC1 cells (Supplementary Figure 5A). Components of the IPAF inflammasome complex were upregulated in SCC2 compared to those in LLC1 cells, whereas components in the membranous system, particularly the plasma membrane, were downregulated in SCC2 cells (Supplementary Figure 5B, 5C). SCC2 cells showed higher expression of COL6A2 and GPNMB, which are characteristic of cell adhesion, and CDKN2C, which nega-

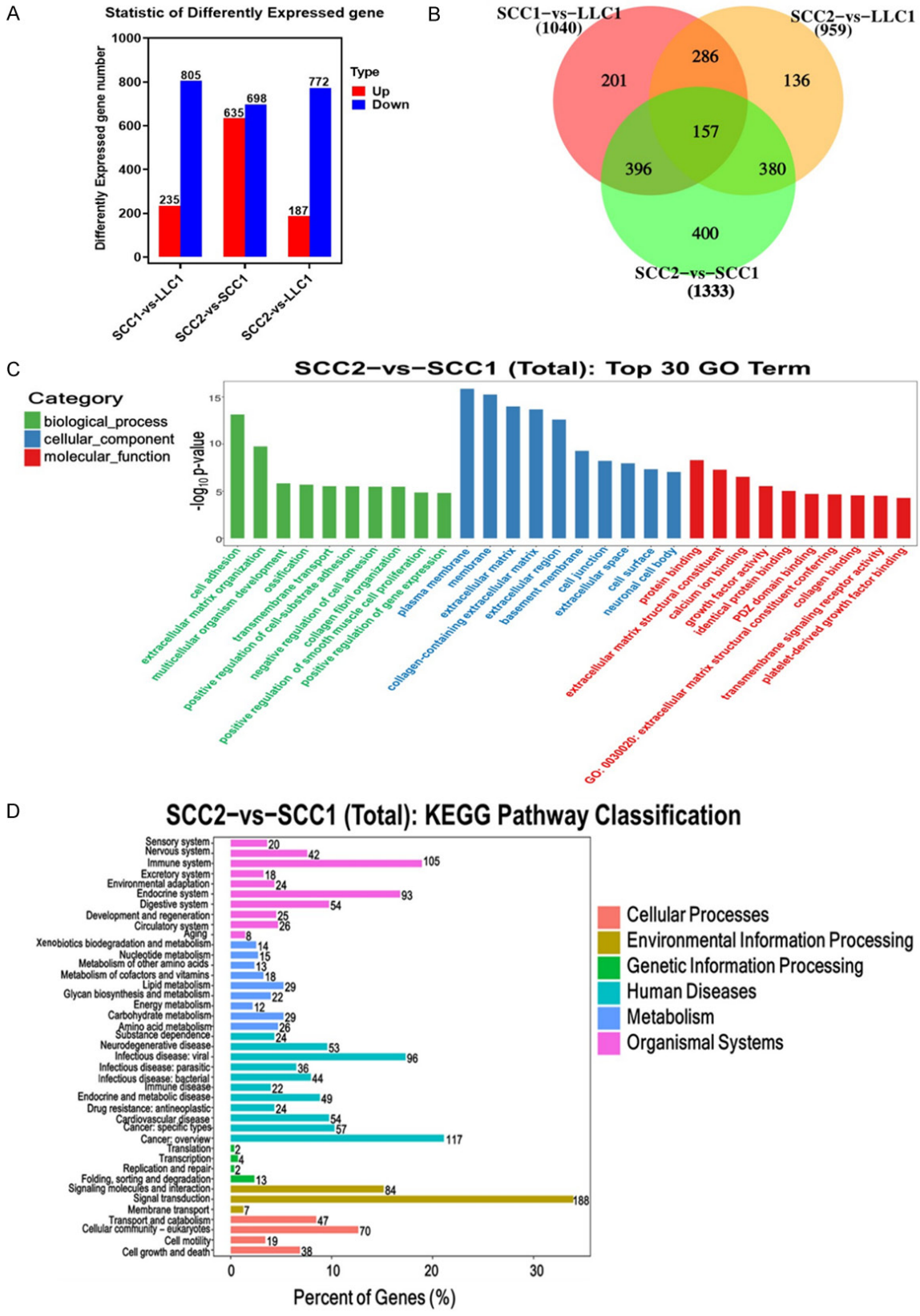

Figure 3. Transcriptomic heterogeneity in LLC1, SCC1, and SCC2 cells. A. Statistical histogram of differentially expressed genes. Up (red) and Down (blue) show the number of up- and downregulated genes, respectively, with significant differences. B. Common and unique differentially expressed genes (DEGs) among different comparison

groups. C. Enriched top 30 GO terms when comparing SCC2 to SCC1 cells (total) by GO enrichment analysis; the y-axis shows the log10-transformed *p*-value. D. Signaling pathway enrichment of DEGs at KEGG Level 2 (KEGG Pathway Classification) in SCC2 compared to that in SCC1 cells.

tively regulates cell growth (Supplementary Figure 3B). This is consistent with the observed morphological changes in SCC2 cells that adhered better to plastic than LLC1 and SCC1 cells.

To identify the key regulators in the mediated morphological and proliferation differences among the three strains, we constructed an association network between 14 differentially expressed TFs and the top 30 enriched GO biological processes according to these DEGs. Most of these are known to negatively regulate cell population proliferation, such as CDKN2C, TGFB1, and HMOX1, and negatively regulate T cell proliferation, such as TNFRSF21, TGFB1, and GPNMB (Supplementary Figure 3C). These transcriptional variations were further validated by quantitative RT-PCR (Supplementary Figure 3D). The primer sequences used for PCR-based Sanger sequencing are listed in Supplementary Table 1.

These results indicate that variations in gene expression arise de novo, in addition to reflecting the selection of pre-existing subclones.

SCC2 causes local immune cell infiltration, proliferation, and activation

Next, we compared the tumor immune infiltrates of LLC1 tumors to those of SCC1 and SCC2 tumors in C57BL/6N mice to better understand the underlying immunological mechanism resulting in the inhibition of tumor growth. Various immune cell subsets and molecules were investigated using FACS analysis on day 18.

There was a pronounced increase in $CD3^+$, $CD8^+$, and NK cell numbers and activation in the SCC2 group, and a significant decrease in MDSC ($CD11b^+Gr\text{-}1^+$) cells. The percentage of $CD3^+$ T cells among CD45-positive cells in the SCC2 group was significantly higher than those in the LLC1 (10.28% vs. 1.26%, P = 0.0004) and SCC1 groups (10.28% vs. 0.64%, P = 0.0002, **Figure 4A**, **4B**). The percentage of $CD3^+CD4^+$ T cells among CD45-positive cells in the SCC2 group was significantly higher than those in the LLC1 (5.45% vs. 0.66%, P = 0.0002) and SCC1 groups (5.45% vs. 0.33%, P = 0.0001, **Figure 4C**, **4D**). The percentage of $CD3^+CD8^+$ T cells among CD45-positive cells in the SCC2 group was significantly higher than those in the LLC1 (2.38% vs. 0.3%, P = 0.0001) and SCC1 groups (2.38% vs. 0.16%, P < 0.0001, **Figure 4E**, **4F**). The percentage of $CD11b^+Gr\text{-}1^+$ cells among CD45-positive cells in the SCC2 group was significantly lower than those in the LLC1 (72.52% vs. 95.12%, P < 0.0001) and SCC1 groups (72.52% vs. 95.44%, P < 0.0001, **Figure 4G**, **4H**).

Next, the activation marker (PD-1) and exhaustion marker ($PD\text{-}1^+Tim\text{-}3^+$) of lymphoid cells were evaluated. An increase in the frequency of $PD\text{-}1^+$ among $CD4^+$ and $CD8^+$ T cells was observed in the SCC2 group; an increase in the frequency of $PD\text{-}1^+Tim\text{-}3^+$ among $CD8^+$ cells (12.74% vs. 3.9% for SCC2 vs. LLC1, P = 0.0146; 12.74% vs. 5.19% for SCC2 vs. SCC1, P = 0.0351) was also observed in the SCC2 group (**Figure 5A-E**). The percentage of NK cells among CD45-positive cells in the SCC2 group was significantly higher than those in the LLC1 (5.69% vs. 1.76%, P = 0.0005) and SCC1 groups (5.69% vs. 0.82%, P < 0.0001, **Figure 5F**). The expression of PD-1 and/or Tim-3 in NK cells did not differ among the three groups (**Figure 5G**, **5H**).

The expression of PD-L1 in CD45-positive cells in the SCC2 group was significantly higher than those in the LLC1 (78.52% vs. 35.74%, P < 0.0001) and SCC1 groups (78.52% vs. 38.36%, P < 0.0001, **Figure 5I**).

TFs validated in vitro were further validated using quantitative RT-PCR in tumor tissues. GPNMB was significantly higher in SCC1 than in LLC1 cells in vitro and lower in SCC1 than in LLC1 cells in vivo. TMEM176B expression was significantly lower in SCC2 than in LLC1 cells in vitro, whereas it was higher in SCC2 than in LLC1 cells in vivo. The in vitro results of GRB10 expression were consistent in vivo (**Figure 6A**).

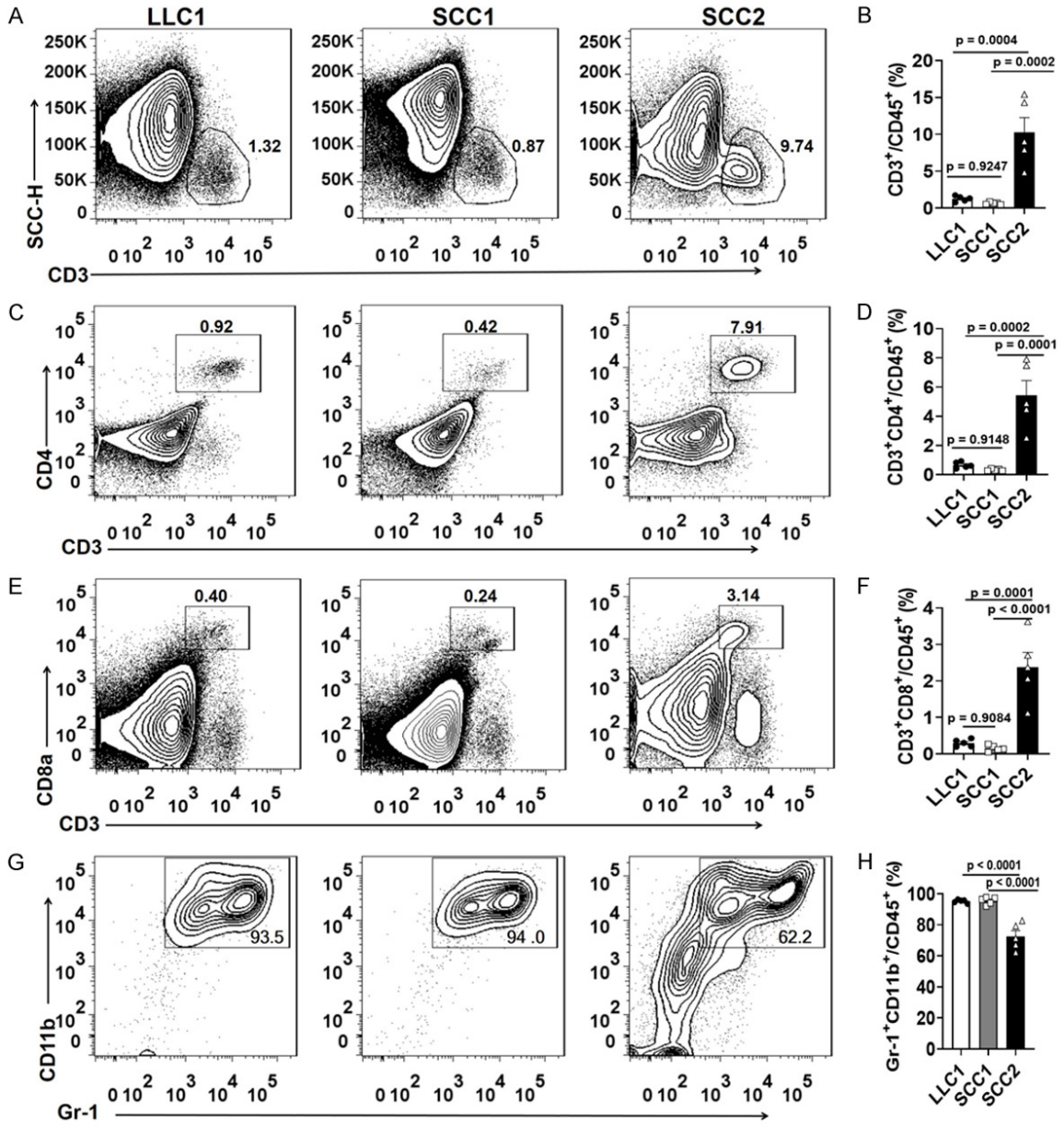

Figure 4. Flow cytometry analysis of immune cell populations in the tumor microenvironment of LLC1, SCC1, and SCC2 tumor bearing mice. Representative plots of $CD3^+$ T (A), $CD3^+CD4^+$ T (C), $CD3^+CD8^+$ T (E), and MDSC ($CD11b^+Gr\text{-}1^+$) (G) cell frequency among CD45-positive cells. Pooled data of $CD3^+$ T (B), $CD3^+CD4^+$ T (D), $CD3^+CD8^+$ T (F), and MDSC ($CD11b^+Gr\text{-}1^+$) (H) cell frequency among CD45-positive cells (n = 5 per group, one-way ANOVA followed by Tukey's multiple comparison test, *P < 0.05; **P < 0.01; ***P < 0.001; ****P < 0.0001).

SCDCLs have poor response to anti-PD-1 therapy

LLC1 has been widely described as being non-responsive to checkpoint blockade immunotherapy [19-21]. The therapeutic efficacy of anti-PD-1 monotherapy was tested in wild-type C57BL/6N mice bearing subcutaneous SCDCL tumors. Compared with control IgG, anti-PD-1 monotherapy did not show any effect on tumor growth (**Figure 6B-D**). These results are consistent with the observation that anti-PD-1 monotherapy was not effective in LLC1 cells.

Histology and lung metastases tumor burden scoring of SCDCLs

Hematoxylin and eosin staining showed no lung metastases in any of the three cell line groups (Supplementary Figure 6).

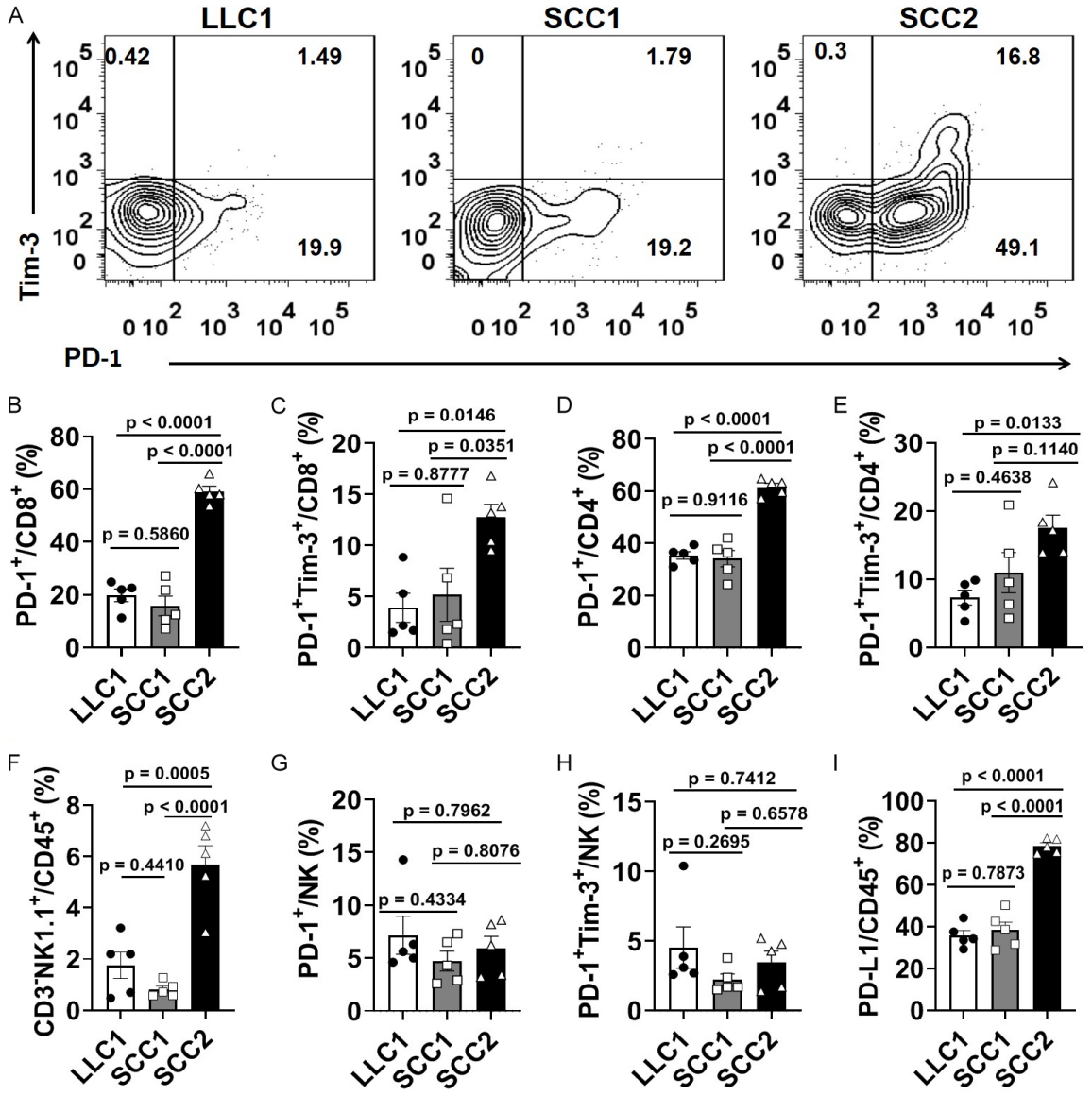

Figure 5. Representative plots of PD-1$^+$ and Tim-3$^+$PD-1$^+$ (A) among CD8$^+$ T cells. Pooled data of PD-1$^+$ (B) and Tim-3$^+$PD-1$^+$ (C) among CD8$^+$ T cells; and PD-1$^+$ (D) and Tim-3$^+$PD-1$^+$ (E) among CD4$^+$ T cells. Pooled data of NK cell frequency among CD45-positive cells (F). Pooled data of PD-1$^+$ (G) and Tim-3$^+$PD-1$^+$ (H) among NK cells; PD-L1 frequency among CD45-positive cells (I) (one-way ANOVA, *P < 0.05; **P < 0.01; ***P < 0.001; ****P < 0.0001).

Discussion

Researchers, recognizing the heterogeneity of cell lines, have established methods to minimize experimental irreproducibility. For example, using cell lines within a defined window to minimize genetic drift, confirming specific mutation/pathway status locally, and using robust statistical standards [8, 9].

Stable segregation of specific subpopulations in tumor cell lines helps to probe primary tumor heterogeneity. In this study, by limiting dilution, we first established SCDCLs from the widely-used mouse cell line LLC1 that demonstrated different genetic and intrinsic proliferative characteristics in vitro. SCDCLs were then subcutaneously inoculated into C57BL/6 mice and their growth observed in vivo. Surprisingly, subclone SCC1 grew the fastest in vivo and relatively slowly in vitro. The opposite pattern was observed in SCC2 cells. In addition, the tumor growth of SCC3 and SCC4 cells was not different, whereas SCC3 cells grew at a significantly slower rate in vitro than SCC4 cells; this phenomenon was also observed in SCC4 and SCC5

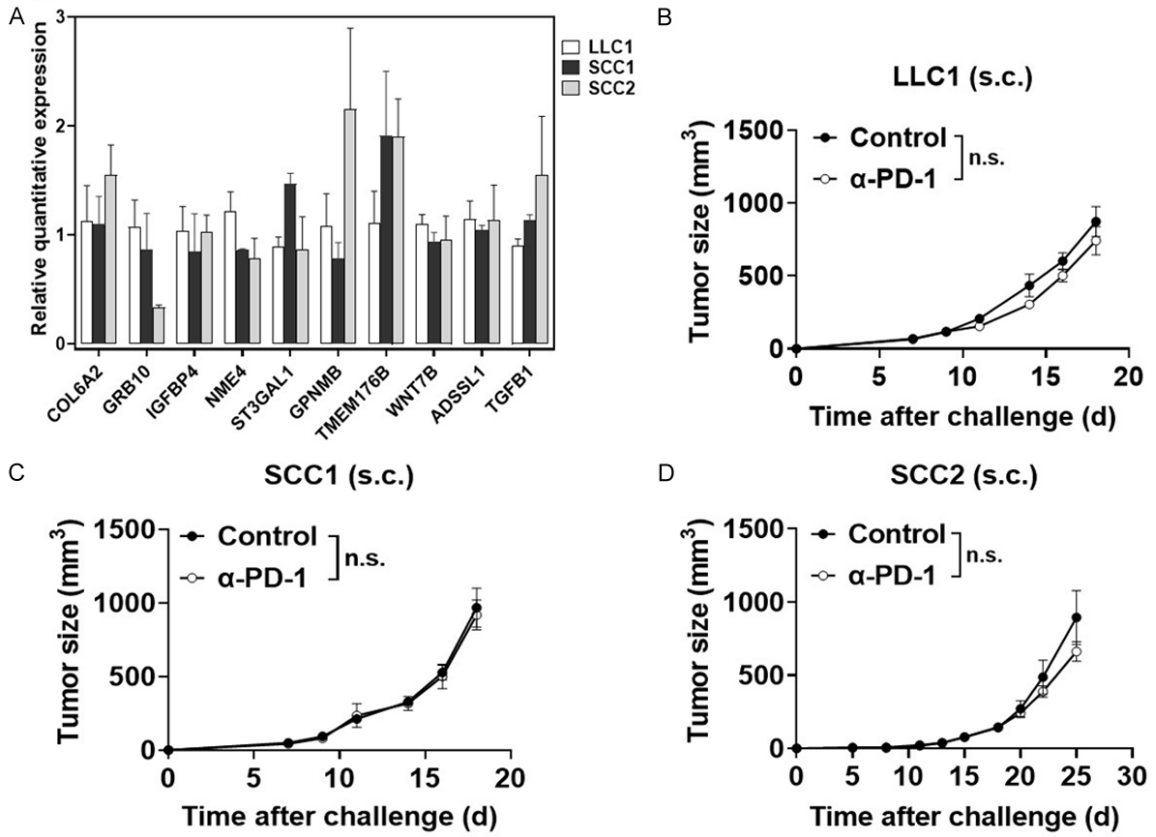

Figure 6. SCDCLs show poor response to anti-PD-1 therapy. A. Selected transcription factors were validated in tumors by quantitative RT-PCR. B-D. SCDCLs have poor response to anti-PD-1 therapy.

cells. This type of subpopulation analysis highlights the importance of considering tumor cell heterogeneity and intrinsic biological characterization, even within tumor cell lines, and may also provide more clinically relevant models for assessing treatment efficacy.

SCC1 and SCC2 cells exhibited differential morphology, growth, and sensitivity to anticancer drugs and xenografts in vivo. WES and transcriptome sequencing analysis show that genetic changes were associated with differential activation of gene expression programs and marked differences in cell membranes, cell adhesion, and proliferation, and that genomic variability has a complex, nonlinear effect on the transcriptome [18, 22]. Beyond the measured genomic variation, under identical culture conditions, SCC1 and SCC2 cells exhibited transcriptomic variation, albeit with an overall similarity in global gene expression profiles. Such transcriptional variation appears transient and flexible in response to environmental stimuli and is partially influenced by DNA alterations. These differences indicate heterogeneity with regard to growth rate, in line with other experimental systems [13, 23, 24], and tied to the proportion of cells with different phenotypes within the same culture. These results help to explain the different biological characteristics of these clones in vitro. The differently expressed genes related to activities, such as cell adhesion, signal transduction, and regulation of cell migration between these two subclones, may be due to intrinsic factors affecting the tumor microenvironment. Our results suggest that GRB10, IGFBP4, and TMEM176B may play a positive role in tumor growth, thereby warranting further investigation.

We analyzed the tumor-infiltrating immune cells in C57BL/6 mice and found that there were more T cells and NK cells but fewer myeloid cells in SCC2 than in SCC1 and LLC1 tumors, which indicates that the growth rate of the cancer cells in immune-complete mice was controlled by the tumor immune environment rather than in vitro growth ability. This is consistent

with the results of Wolf et al. [25], who showed reduced growth in vitro and increased tumor growth in vivo. In addition, a recent study showed doubling time differences between HeLa cell variants [18]. The complex inter-relationships that exist between cells in vivo are lost when cell lines are cultured on plastic in two dimensions; however, two-dimensional culture remains the most favored mechanism for in vitro studies in lung cancer research [26-28]. In addition, cell lines are often sensitive to culture conditions, particularly the inclusion of growth factors that can alter the cell phenotype, resulting in inappropriate pathway activation or differentiation [29-34]. The differently expressed genes TGFB1, TNFRSF21, and GPNMB between these two subclones are related to T cell proliferation, and the genes TMEM176A and TMEM176B are concerned with dendritic cell differentiation. These inconsistencies may be useful in explaining the difference in tumor-infiltrating immune cells between the groups.

The efficacy of anti-PD-1/PD-L1 therapy is related to the TIL status and PD-L1 expression in tumor cells in non-small cell lung cancer [8]. There was a pronounced increase in $CD3^+$, $CD8^+$, and NK cell numbers and activation, and a significant decrease in MDSC ($CD11b^+Gr\text{-}1^+$) cells in the SCC2 group, whereas the TIL status did not predict response to anti-PD-1 therapy in this study. Other suppressors promote immune tolerance including non-PD-1/PD-L1 checkpoint molecules, such as LAG-3, TIM-3, and TIGIT; immunosuppressive pathways, such as adenosine and indoleamine 2, 3-dioxygenase; and the tumor mutation burden [35, 36]. Working together, they all create a complex immunosuppressive tumor microenvironment, meaning the two subclones did not show effect on tumor growth to anti-PD-1 therapy.

Subcutaneously, LLC1 tumors spontaneously metastasize to the lungs and, in some cases, the liver via the vasculature [12, 37, 38], often with significant inter-mouse variability. However, in this study, we did not find lung metastases, which may be related to tumor volumes not exceeding 2000 mm^3 and different inoculation methods [12]. In the present study, C57BL/6N Mice were sacrificed 18 days after receiving 1×10^6 tumor cells via subcutaneous injection into the right flank. Lung metastases were typically not detectable in the nude mouse model with subcutaneous LLC tumors until the tumors grew beyond 1000 mm^3 [13]. However, in other studies, 5×10^5 viable tumor cells were injected intramuscularly into the hind leg, 10^5 or 2×10^5 viable tumor cells were injected into the lateral vein of the tail, or 10^5 tumor cells were implanted in the footpad, and the mice were euthanized between 21 and 91 days [14] to allow analysis of spontaneous metastases for up to seven months. Moreover, the median number of metastases was positively correlated with the median weight and average growth rate of the primary tumors. Furthermore, heterogeneity in metastatic spread likely originated from small differences in tumor placement and access to vasculature [13]. In addition, a significant increase in metastatic potential was once observed after a prolonged culture period of that same clone [14]. However, in the present study, the SCDCLs were cultured and passaged in vitro no more than eight times.

The genetic and immunological characterizations we observed may have intriguing implications for understanding the biology of LLC1 cells. First, we identified two distinct groups of clones with different proliferation and renewal potentials, providing experimental evidence of the existence of heterogeneity in unperturbed cancer cell lines. Second, there are characteristic transcriptional differences underlying the different growth ratios, and multiple genes are involved in these differences. Third, each clonal population from LLC1 expresses a set of intrinsic genes that determine its specific functional behavior and responsiveness to the tumor environment. Finally, the in vivo growth of subclones derived from LLC1 was determined by the tumor microenvironment instead of the intrinsic proliferative characteristics of cells. Although further studies are needed to better understand these differences, both mouse models are important for human lung cancer research. A major limitation of this study is that it only included the LLC1 cell line. Similar studies should be conducted for other cancer types.

Understanding the genetic, epigenetic, and immunological heterogeneity of cancer cells is crucial for the design of more effective cancer therapies and helps to explain how cancer disseminates and progresses [39]. Importantly, recognizing the genetic and immunological characterization of LLC1 cells, whether in vitro or in vivo, helps researchers improve the reporting and reproducibility of preclinical cancer research [40, 41].

Conclusions

Our results indicate that the in vivo growth of LLC1 cells is determined by the tumor microenvironment rather than their intrinsic proliferative ability, which is meaningful for understanding the relationship between cancer growth and the immune system to design more reasonable treatments.

Acknowledgements

We thank Drs. Qing Wang, and Yu-Guo Wu from Shanghai OE Biotech. Co., Ltd., Shanghai, China, for their technical support in RNA-sequencing and whole exome sequencing. We thank all the investigators for their participation from the immunotherapy department of Henan Cancer Center Hospital for their contributions. We would like to thank Editage (www.editage.cn) for English language editing. This project was supported by The National Natural Science Foundation of China (No. 82172700), National Cancer Center Climbing Fund (NCC201916B-03), Provincial-ministerial Co-construction Project of Henan Province Science and Technology Key Point Tackling Plan (SBGJ202102064), and Henan Provincial Scientific and Technological Project (222102310363, 222102310677). This study was approved by the Institute Ethical Committee of the Affiliated Cancer Hospital of Zhengzhou University, China.

Disclosure of conflict of interest

None.

Address correspondence to: Drs. Quan-Li Gao and Zi-Bing Wang, Department of Immunotherapy, The Affiliated Cancer Hospital of Zhengzhou University & Henan Cancer Hospital, 127 Dongming Road, Zhengzhou 450008, Henan, P. R. China. Tel: +86-371-65587199; E-mail: zlyygql0855@zzu.edu.cn (QLG); Tel: +86-371-65587099; E-mail: zlyywzb2118@zzu.edu.cn (ZBW); Dr. Long Yuan, Department of General Surgery, The Affiliated Cancer Hospital of Zhengzhou University & Henan Cancer Hospital, Zhengzhou 450008, Henan, P. R. China. Tel: +86-371-65587951; E-mail: zlyyyuanlong1255@zzu.edu.cn

References

[1] Siegel RL, Miller KD, Fuchs HE and Jemal A. Cancer statistics, 2022. CA Cancer J Clin 2022; 72: 7-33.

[2] Raso MG, Bota-Rabassedas N and Wistuba II. Pathology and classification of SCLC. Cancers (Basel) 2021; 13: 820.

[3] Wang M, Herbst RS and Boshoff C. Toward personalized treatment approaches for non-small-cell lung cancer. Nat Med 2021; 27: 1345-1356.

[4] Liu Y, Mi Y, Mueller T, Kreibich S, Williams EG, Van Drogen A, Borel C, Frank M, Germain PL, Bludau I, Mehnert M, Seifert M, Emmenlauer M, Sorg I, Bezrukov F, Bena FS, Zhou H, Dehio C, Testa G, Saez-Rodriguez J, Antonarakis SE, Hardt WD and Aebersold R. Multi-omic measurements of heterogeneity in HeLa cells across laboratories. Nat Biotechnol 2019; 37: 314-322.

[5] Cheng Y, Shi D, Xu Z, Gao Z, Si Z, Zhao Y, Ye R, Fu Z, Fu W, Yang T, Xiu Y, Lin Q and Cheng D. (124)I-labeled monoclonal antibody and fragment for the noninvasive evaluation of tumor PD-L1 expression in vivo. Mol Pharm 2022; 19: 3551-3562.

[6] Olivo Pimentel V, Marcus D, van der Wiel AM, Lieuwes NG, Biemans R, Lieverse RI, Neri D, Theys J, Yaromina A, Dubois LJ and Lambin P. Releasing the brakes of tumor immunity with anti-PD-L1 and pushing its accelerator with L19-IL2 cures poorly immunogenic tumors when combined with radiotherapy. J Immunother Cancer 2021; 9: e001764.

[7] To K, Fong W and Cho W. Immunotherapy in treating EGFR-mutant lung cancer: current challenges and new strategies. Front Oncol 2021; 11: 635007.

[8] Shirasawa M, Yoshida T, Shimoda Y, Takayanagi D, Shiraishi K, Kubo T, Mitani S, Matsumoto Y, Masuda K, Shinno Y, Okuma Y, Goto Y, Horinouchi H, Ichikawa H, Kohno T, Yamamoto N, Matsumoto S, Goto K, Watanabe SI, Ohe Y and Motoi N. Differential immune-related microenvironment determines programmed cell death protein-1/programmed death-ligand 1 blockade efficacy in patients with advanced NSCLC. J Thorac Oncol 2021; 16: 2078-2090.

[9] Ben-David U, Siranosian B, Ha G, Tang H, Oren Y, Hinohara K, Strathdee CA, Dempster J, Lyons NJ, Burns R, Nag A, Kugener G, Cimini B, Tsvetkov P, Maruvka YE, O'Rourke R, Garrity A, Tubelli AA, Bandopadhayay P, Tsherniak A, Vazquez F, Wong B, Birger C, Ghandi M, Thorner AR, Bittker JA, Meyerson M, Getz G, Beroukhim R and Golub TR. Genetic and transcriptional evolution alters cancer cell line drug response. Nature 2018; 560: 325-330.

[10] Hynds RE, Vladimirou E and Janes SM. The secret lives of cancer cell lines. Dis Model Mech 2018; 11: dmm037366.

[11] Cleary AS, Leonard TL, Gestl SA and Gunther EJ. Tumour cell heterogeneity maintained by

cooperating subclones in Wnt-driven mammary cancers. Nature 2014; 508: 113-7.
[12] Pozo K, Kelenis DP, Minna JD and Johnson JE. Different originating cells underlie intertumoral heterogeneity in lung neuroendocrine tumors. Cancer Discov 2018; 8: 1216-1218.
[13] Fitzgerald JE, Byrd BK, Patil RA, Strawbridge RR, Davis SC, Bellini C and Niedre M. Heterogeneity of circulating tumor cell dissemination and lung metastases in a subcutaneous Lewis lung carcinoma model. Biomed Opt Express 2020; 11: 3633-3647.
[14] van Lamsweerde AL, Henry N and Vaes G. Metastatic heterogeneity of cells from Lewis lung carcinoma. Cancer Res 1983; 43: 5314-20.
[15] Sun C, Nagaoka K, Kobayashi Y, Nakagawa H, Kakimi K and Nakajima J. Neoantigen dendritic cell vaccination combined with anti-CD38 and CpG elicits anti-tumor immunity against the immune checkpoint therapy-resistant murine lung cancer cell line LLC1. Cancers (Basel) 2021; 13: 5508.
[16] Žilionytė K, Bagdzevičiūtė U, Mlynska A, Urbštaitė E, Paberalė E, Dobrovolskienė N, Krasko JA and Pašukonienė V. Functional antigen processing and presentation mechanism as a prerequisite factor of response to treatment with dendritic cell vaccines and anti-PD-1 in preclinical murine LLC1 and GL261 tumor models. Cancer Immunol Immunother 2022; 71: 2691-2700.
[17] Veiseh M, Kwon DH, Borowsky AD, Tolg C, Leong HS, Lewis JD, Turley EA and Bissell MJ. Cellular heterogeneity profiling by hyaluronan probes reveals an invasive but slow-growing breast tumor subset. Proc Natl Acad Sci U S A 2014; 111: E1731-9.
[18] Holliday DL and Speirs V. Choosing the right cell line for breast cancer research. Breast Cancer Res 2011; 13: 215.
[19] Wang K, Gu Y, Liao Y, Bang S, Donnelly CR, Chen O, Tao X, Mirando AJ, Hilton MJ and Ji RR. PD-1 blockade inhibits osteoclast formation and murine bone cancer pain. J Clin Invest 2020; 130: 3603-3620.
[20] Qin J, Zhang X, Tan B, Zhang S, Yin C, Xue Q, Zhang Z, Ren H, Chen J, Liu M, Qian M and Du B. Blocking P2X7-mediated macrophage polarization overcomes treatment resistance in lung cancer. Cancer Immunol Res 2020; 8: 1426-1439.
[21] Johnson AM, Bullock BL, Neuwelt AJ, Poczobutt JM, Kaspar RE, Li HY, Kwak JW, Hopp K, Weiser-Evans MCM, Heasley LE, Schenk EL, Clambey ET and Nemenoff RA. Cancer cell-intrinsic expression of MHC class II regulates the immune microenvironment and response to anti-PD-1 therapy in lung adenocarcinoma. J Immunol 2020; 204: 2295-2307.
[22] Niehr F, Eder T, Pilz T, Konschak R, Treue D, Klauschen F, Bockmayr M, Türkmen S, Jöhrens K, Budach V and Tinhofer I. Multilayered omics-based analysis of a head and neck cancer model of cisplatin resistance reveals intratumoral heterogeneity and treatment-induced clonal selection. Clin Cancer Res 2018; 24: 158-168.
[23] Kiger N. Heterogeneity in surface antigen of cell lines and clones from a murine carcinoma. Int J Cancer 1985; 35: 129-34.
[24] Quinn JJ, Jones MG, Okimoto RA, Nanjo S, Chan MM, Yosef N, Bivona TG and Weissman JS. Single-cell lineages reveal the rates, routes, and drivers of metastasis in cancer xenografts. Science 2021; 371: eabc1944.
[25] Wolf Y, Bartok O, Patkar S, Eli GB, Cohen S, Litchfield K, Levy R, Jiménez-Sánchez A, Trabish S, Lee JS, Karathia H, Barnea E, Day CP, Cinnamon E, Stein I, Solomon A, Bitton L, Pérez-Guijarro E, Dubovik T, Shen-Orr SS, Miller ML, Merlino G, Levin Y, Pikarsky E, Eisenbach L, Admon A, Swanton C, Ruppin E and Samuels Y. UVB-induced tumor heterogeneity diminishes immune response in melanoma. Cell 2019; 179: 219-235, e21.
[26] Sottoriva A, Kang H, Ma Z, Graham TA, Salomon MP, Zhao J, Marjoram P, Siegmund K, Press MF, Shibata D and Curtis C. A Big Bang model of human colorectal tumor growth. Nat Genet 2015; 47: 209-16.
[27] Salcedo A, Tarabichi M, Espiritu SMG, Deshwar AG, David M, Wilson NM, Dentro S, Wintersinger JA, Liu LY, Ko M, Sivanandan S, Zhang H, Zhu K, Ou Yang TH, Chilton JM, Buchanan A, Lalansingh CM, P'ng C, Anghel CV, Umar I, Lo B and Zou W; DREAM SMC-Het Participants, Simpson JT, Stuart JM, Anastassiou D, Guan Y, Ewing AD, Ellrott K, Wedge DC, Morris Q, Van Loo P and Boutros PC. A community effort to create standards for evaluating tumor subclonal reconstruction. Nat Biotechnol 2020; 38: 97-107.
[28] Williams MJ, Werner B, Heide T, Curtis C, Barnes CP, Sottoriva A and Graham TA. Quantification of subclonal selection in cancer from bulk sequencing data. Nat Genet 2018; 50: 895-903.
[29] Liu LY, Bhandari V, Salcedo A, Espiritu SMG, Morris QD, Kislinger T and Boutros PC. Quantifying the influence of mutation detection on tumour subclonal reconstruction. Nat Commun 2020; 11: 6247.
[30] Turajlic S, Sottoriva A, Graham T and Swanton C. Resolving genetic heterogeneity in cancer. Nat Rev Genet 2019; 20: 404-416.
[31] Meyer M, Reimand J, Lan X, Head R, Zhu X, Kushida M, Bayani J, Pressey JC, Lionel AC, Clarke ID, Cusimano M, Squire JA, Scherer SW,

Bernstein M, Woodin MA, Bader GD and Dirks PB. Single cell-derived clonal analysis of human glioblastoma links functional and genomic heterogeneity. Proc Natl Acad Sci U S A 2015; 112: 851-6.

[32] Demmers LC, Kretzschmar K, Van Hoeck A, Bar-Epraïm YE, van den Toorn HWP, Koomen M, van Son G, van Gorp J, Pronk A, Smakman N, Cuppen E, Clevers H, Heck AJR and Wu W. Single-cell derived tumor organoids display diversity in HLA class I peptide presentation. Nat Commun 2020; 11: 5338.

[33] Li S, Simoni Y, Zhuang S, Gabel A, Ma S, Chee J, Islas L, Cessna A, Creaney J, Bradley RK, Redwood A, Robinson BW and Newell EW. Characterization of neoantigen-specific T cells in cancer resistant to immune checkpoint therapies. Proc Natl Acad Sci U S A 2021; 118: e2025570118.

[34] Kinker GS, Greenwald AC, Tal R, Orlova Z, Cuoco MS, McFarland JM, Warren A, Rodman C, Roth JA, Bender SA, Kumar B, Rocco JW, Fernandes PACM, Mader CC, Keren-Shaul H, Plotnikov A, Barr H, Tsherniak A, Rozenblatt-Rosen O, Krizhanovsky V, Puram SV, Regev A and Tirosh I. Pan-cancer single-cell RNA-seq identifies recurring programs of cellular heterogeneity. Nat Genet 2020; 52: 1208-1218.

[35] Smyth MJ, Ngiow SF, Ribas A and Teng MW. Combination cancer immunotherapies tailored to the tumour microenvironment. Nat Rev Clin Oncol 2016; 13: 143-158.

[36] Li HY, McSharry M, Bullock B, Nguyen TT, Kwak J, Poczobutt JM, Sippel TR, Heasley LE, Weiser-Evans MC, Clambey ET and Nemenoff RA. The tumor microenvironment regulates sensitivity of murine lung tumors to PD-1/PD-L1 antibody blockade. Cancer Immunol Res 2017; 5: 767-777.

[37] Zheng M, Lu R, Che X, Li J, Zhou C, Wang L, Xu Q, Cao H, Li Q and Yao Z. Tyroservatide therapy for tumor growth, invasion and metastasis of Lewis lung carcinoma and human lung carcinoma A549. Oncology 2006; 70: 418-26.

[38] Yao Z, Zhang J, Zhang B, Liang G, Chen X, Yao F, Xu X, Wu H, He Q, Ding L and Yang B. Imatinib prevents lung cancer metastasis by inhibiting M2-like polarization of macrophages. Pharmacol Res 2018; 133: 121-131.

[39] Braun R, Anthuber L, Hirsch D, Wangsa D, Lack J, McNeil NE, Heselmeyer-Haddad K, Torres I, Wangsa D, Brown MA, Tubbs A, Auslander N, Gertz EM, Brauer PR, Cam MC, Sackett DL, Habermann JK, Nussenzweig A, Ruppin E, Zhang Z, Rosenberg DW and Ried T. Single-cell-derived primary rectal carcinoma cell lines reflect intratumor heterogeneity associated with treatment response. Clin Cancer Res 2020; 26: 3468-3480.

[40] Janiszewska M, Tabassum DP, Castaño Z, Cristea S, Yamamoto KN, Kingston NL, Murphy KC, Shu S, Harper NW, Del Alcazar CG, Alečković M, Ekram MB, Cohen O, Kwak M, Qin Y, Laszewski T, Luoma A, Marusyk A, Wucherpfennig KW, Wagle N, Fan R, Michor F, McAllister SS and Polyak K. Subclonal cooperation drives metastasis by modulating local and systemic immune microenvironments. Nat Cell Biol 2019; 21: 879-888.

[41] Sanmamed MF and Chen L. A paradigm shift in cancer immunotherapy: from enhancement to normalization. Cell 2018; 175: 313-326.

Life science ethics review committee of Zhengzhou University

Ethical review report

Project： Study of p120-ctn on the dual regulation of PD-L1 expression and tumor microenvironment in non-small cell lung cancer

Principal Investigator：Quanli Gao

Ethical review opinions:

After the review by the life science ethics review committee of Zhengzhou University, the research content and process of the project comply with the ethical requirements on biomedical research issued by the international and national governments, and the project approved to apply for the 2021 national natural science foundation project.

郑州大学生命科学伦理审查委员会

Life science ethics review committee of Zhengzhou University

18 March, 2021

Supplementary Table 1. Primer sequences of selected genes

Num	Gene Symbol	Forward primer (5→3)	Reverse primer (5→3)	Product length (bp)
1	ACTB	CCCACTTCTCTCTAAGGAGAAT	TACACGAAAGCAATGCTATCAC	77
2	COL6A2	CCTCCTTCACTAAGAGCCTAC	CTGCGTCATGTTAGCCAAT	83
3	GRB10	GTCTTGGGCTTCAAGTACTAAT	GTATCAGTATCAGACTGCATGT	91
4	IGFBP4	GTACATTGATGCACGGGC	CTCTCATCCTTGTCAGAGGT	91
5	NME4	GGGACTGTGATACAACGC	GCAAGGATGCTTTCTGGT	83
6	ST3GAL1	AGTTGTAGGAAACTCCGGT	TGTTCATCCTCAGCACAAAG	83
7	GPNMB	TCCCGATCACATGAGAGAGCA	CCTCCTCCACACTGGATAC	91
8	TMEM176B	GCTGTGCTCTTGGAGTATG	CAACTCCAGCTAGAATTGCC	102
9	WNT7B	TGCCTTCACCTATGCCATCA	CAATTGCTCAGATTGCCCT	81
10	ADSSL1	GGCACACAGTAGTGGTGGA	CAATGAATGACACGGCCT	87
11	TGFB1	CTGCAAGACCATCGACAT	GAGCCTTAGTTTGGACAGGA	82

Supplementary Table 2. Reagent or resource

Reagent or resource	Source	Identifier
Antibodies		
Rat monoclonal anti-CD45 Pacific Blue™, clone 30-F11, anti-mouse	BioLegend	Cat# 103126, RRID: AB_493535
Rat monoclonal anti-CD355 (NKp46) FITC, clone 29A1.4, anti-mouse	Biolegend	Cat# 137606, RRID: AB_2298210
Rat monoclonal anti-CD3e PE, clone eBio500A2, anti-mouse	Thermo Fisher Scientific	Cat# 12-0033-83, RRID: AB_842787
Rat monoclonal anti-CD366 (Tim-3) PE, clone RMT3-23, anti-mouse	Biolegend	Cat# 119703, RRID: AB_345377
Rat monoclonal anti-CD279 (PD-1), clone 29F.1A12, anti-mouse	Biolegend	Cat# 135210, RRID: AB_2159183
Rat monoclonal IgG2b, kappa Isotype Ctrl APC, clone RTK4530, anti-mouse	Biolegend	Cat# 400612, RRID: AB_326556
Rat monoclonal anti-CD4 FITC, clone RM4-5, anti-mouse	Biolegend	Cat# 100510, RRID: AB_312713
Rat monoclonal anti-CD8a PE-Cy7, clone 53-6.7, anti-mouse	Thermo Fisher Scientific	Cat# 25-0081-82, RRID: AB_469584
Syrian Hamster monoclonal anti-CD3e Pacific Blue, clone eBio500A2, anti-mouse	BD Biosciences	Cat# 558214, RRID: AB_397063
Rat monoclonal anti-CD3 Brilliant Violet 605, clone 100237, anti-mouse	Biolegend	Cat# 100237, RRID: AB_2562039
Rat monoclonal anti-Foxp3 APC, clone FJK-16s, anti-mouse	Thermo Fisher Scientific	Cat# 17-5773-82, RRID: AB_469457
Rat monoclonal anti-CD45 APC, clone 30-F11, anti-mouse	Biolegend	Cat# 103112, RRID: AB_312977
Rat monoclonal anti-Ly-6G/Ly-6C (Gr-1) FITC, clone RB6-8C5, anti-mouse	Biolegend	Cat# 108406, RRID: AB_313371
Rat monoclonal anti-CD8b (Ly-3) PE-Cy7, clone YTS156.7.7, anti-mouse	Biolegend	Cat# 126615, RRID: AB_2562776
Rat monoclonal anti-CD11b PE, clone M1/70, anti-mouse	Biolegend	Cat# 101208, RRID: AB_312791
Rat monoclonal anti-CD274 (PD-L1) APC, clone 10F.9G2, anti-mouse	Biolegend	Cat# 124312, RRID: AB_10612741
Rat monoclonal anti-NK1.1 FITC, clone PK136, anti-mouse	Thermo Fisher Scientific	Cat# 11-5941-82, RRID: AB_465318
InVivoPlus mouse IgG2a isotype control antibody, clone C1.18.4	BioXCell	Cat# BE0085, RRID: AB_1107771
InVivoPlus anti-mouse PD-1 antibody, clone 29F.1A12	BioXCell	Cat# BE0273, RRID: AB_2687796

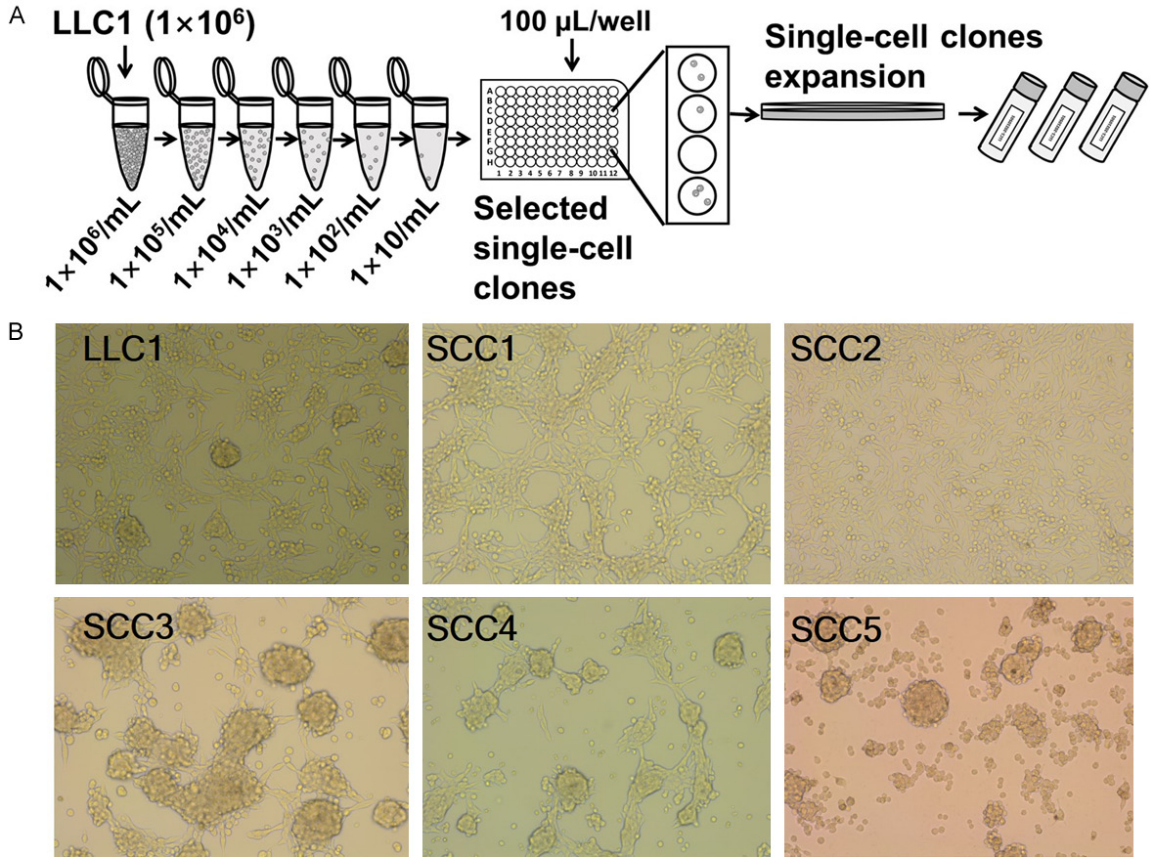

Supplementary Figure 1. Clonal populations derived from LLC1 cells vary in morphology. A. Schematic workflow for single-cell clonal populations derived from LLC1 cells. B. Microscopic images of the SCDCLs showing morphological differences among them (100 ×).

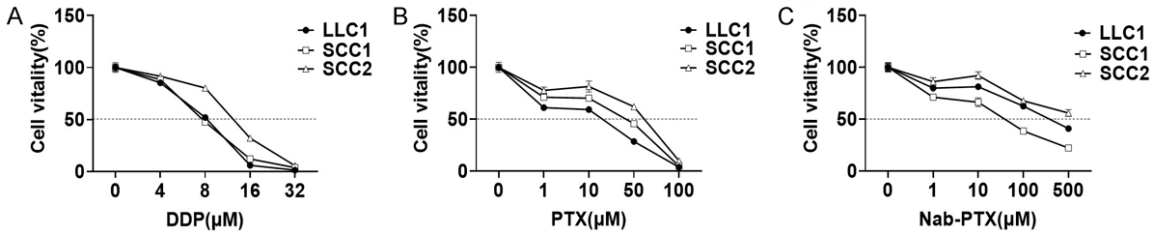

Supplementary Figure 2. SCDCLs Respond Differently to Cytotoxic Drugs. IC50 curve of SCDCLs to DDP (A), PTX (B), Nab-PTX (C).

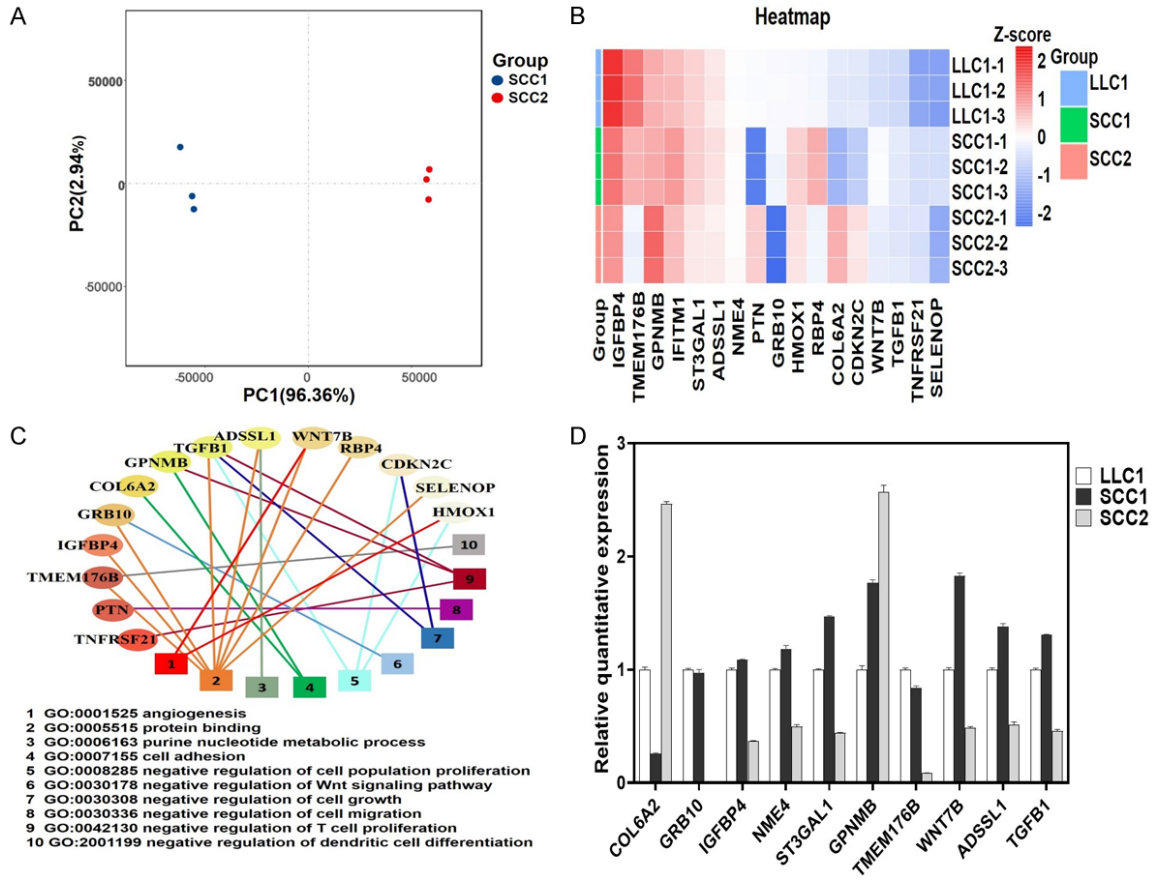

Supplementary Figure 3. Transcriptional analysis of LLC1, SCC1, and SCC2 cells. A. Principal component analysis (PCA). var., variation. B. Heatmap of DEGs selected from the GO enrichment category for all the samples. Scale from blue to red indicates low to high expression levels. C. Involvement network between selected DEGs and biological processes. D. Selected transcription factors were validated using quantitative RT-PCR.

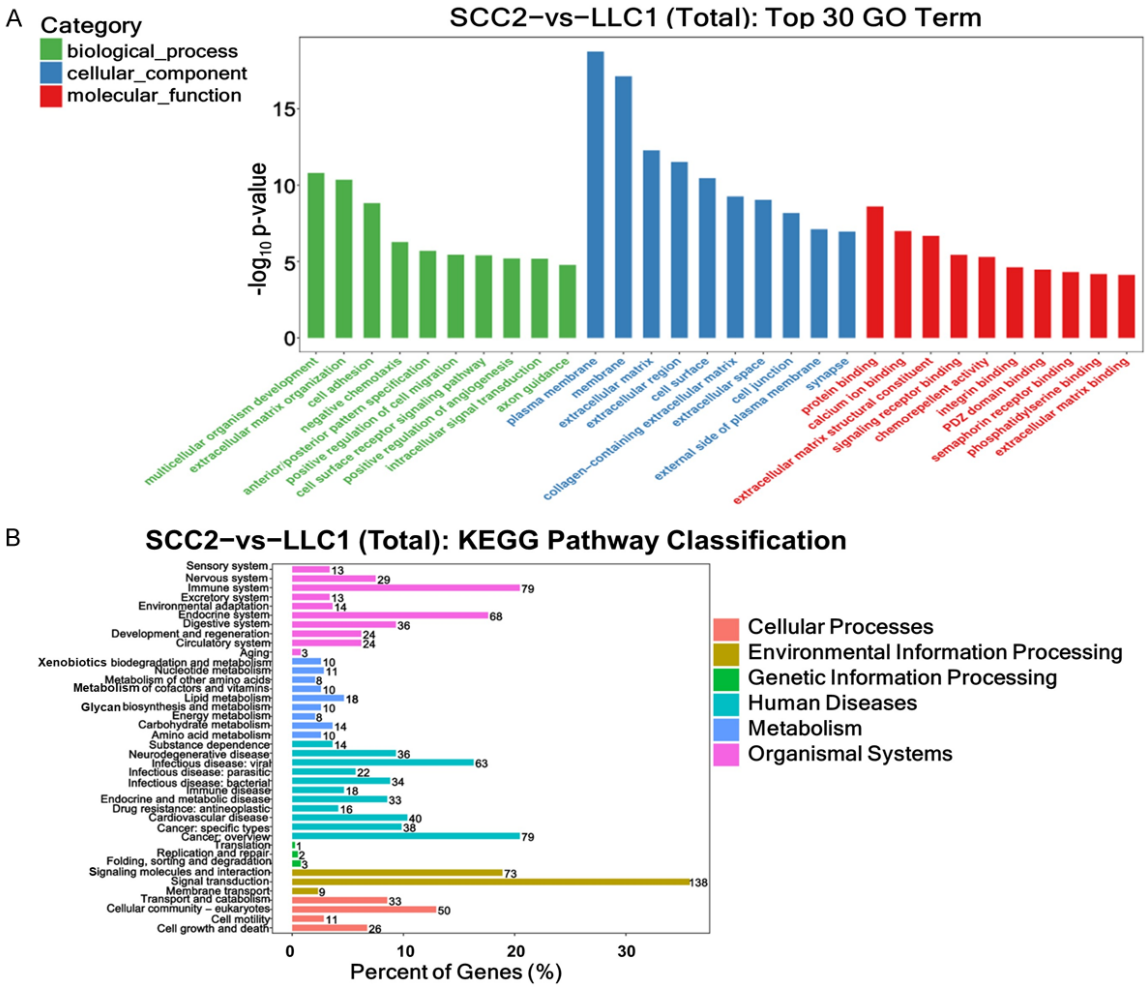

Supplementary Figure 4. A. Enriched top 30 GO terms between SCC2 and LLC1 (total) by GO enrichment analysis, the y-axis shows the log10-transformed *p*-value. B. Signaling pathway enrichment of differentially expressed genes at KEGG Level 2 (KEGG pathway classification) in SCC2 compared to that in LLC1 cells.

A

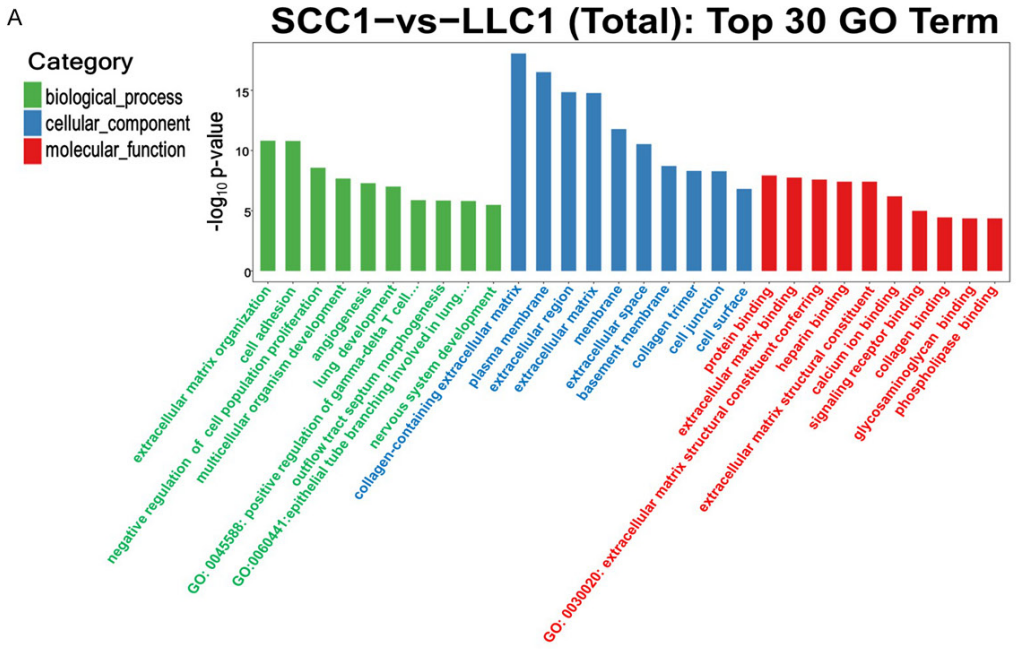
SCC1−vs−LLC1 (Total): Top 30 GO Term
Category
biological_process
cellular_component
molecular_function
-log10 p-value
0
5
10
15
extracellular matrix organization
cell adhesion
cell population proliferation
multicellular organism development
negative regulation of
angiogenesis
lung development
GO: 0045598: positive regulation of gamma-delta T cell...
outflow tract septum morphogenesis
GO:0060441:epithelial tube branching involved in lung...
nervous system development
collagen-containing extracellular matrix
plasma membrane
extracellular region
extracellular matrix
membrane
extracellular space
basement membrane
collagen trimer
cell junction
cell surface
protein binding
extracellular matrix binding
GO: 0030020: extracellular matrix structural constituent conferring
heparin binding
extracellular matrix structural constituent
calcium ion binding
signaling receptor binding
collagen binding
glycosaminoglycan binding
phospholipase binding

B

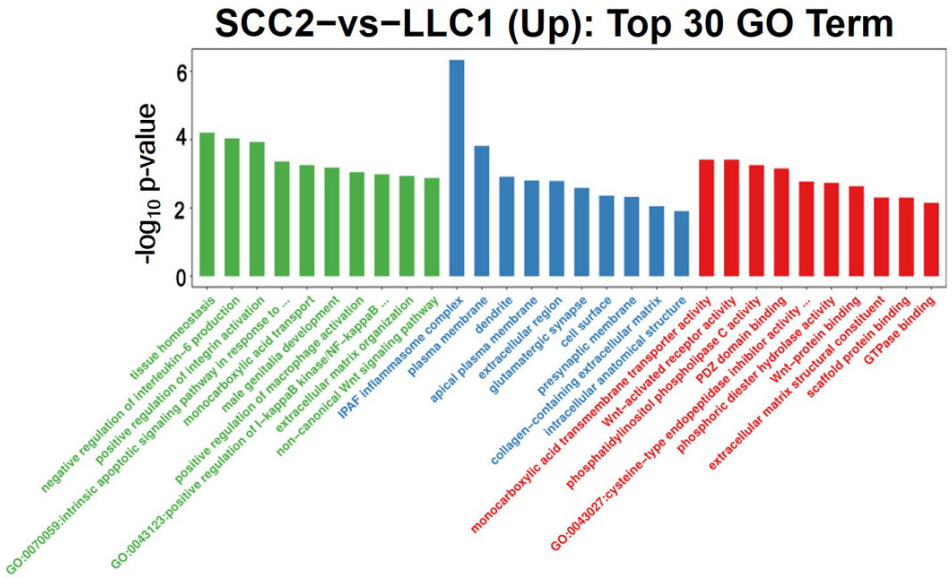
SCC2−vs−LLC1 (Up): Top 30 GO Term
-log10 p-value
0
2
4
6
tissue homeostasis
negative regulation of interleukin-6 production
positive regulation of integrin activation
GO:0070059:intrinsic apoptotic signaling pathway in response to ...
monocarboxylic acid transport
male genitalia development
positive regulation of macrophage activation
GO:0043123:positive regulation of I−kappaB kinase/NF−kappaB ...
extracellular matrix organization
non−canonical Wnt signaling pathway
IPAF inflammasome complex
plasma membrane
apical plasma membrane
dendrite
extracellular region
cell surface
glutamatergic synapse
presynaptic membrane
collagen−containing extracellular matrix
intracellular anatomical structure
Wnt−activated receptor activity
monocarboxylic acid transmembrane transporter activity
phosphatidylinositol phospholipase C activity
GO:0043027:cysteine−type endopeptidase inhibitor activity ...
PDZ domain binding
phosphoric diester hydrolase activity
Wnt−protein binding
extracellular matrix structural constituent
scaffold protein binding
GTPase binding

C

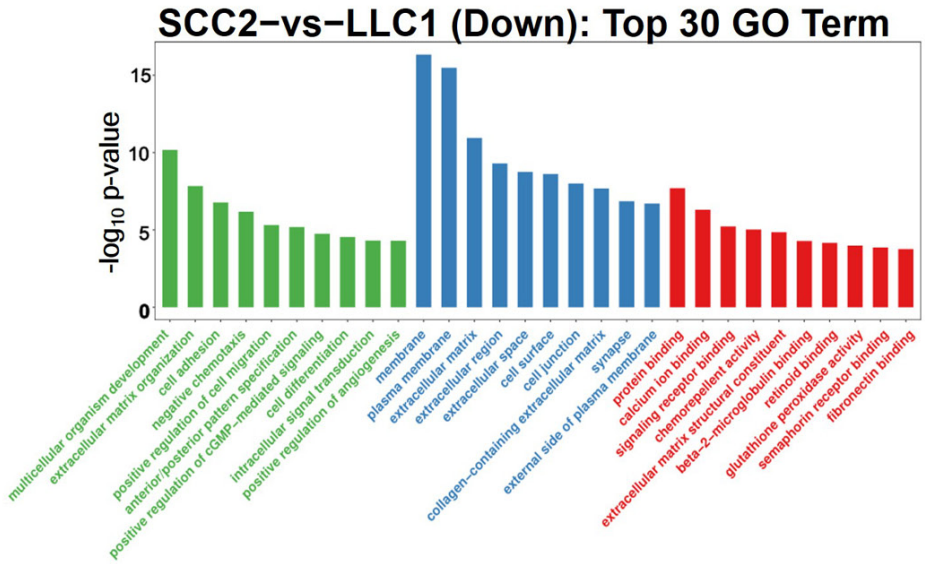
SCC2−vs−LLC1 (Down): Top 30 GO Term
-log10 p-value
0
5
10
15
multicellular organism development
extracellular matrix organization
cell adhesion
negative chemotaxis
positive regulation of cell migration
anterior/posterior pattern specification
positive regulation of cGMP−mediated signaling
cell differentiation
intracellular signal transduction
positive regulation of angiogenesis
membrane
plasma membrane
extracellular matrix
extracellular region
extracellular space
cell surface
cell junction
collagen−containing extracellular matrix
synapse
external side of plasma membrane
protein binding
calcium ion binding
signaling receptor binding
chemorepellent activity
extracellular matrix structural constituent
beta−2−microglobulin binding
retinoid binding
glutathione peroxidase activity
semaphorin receptor binding
fibronectin binding

Supplementary Figure 5. Enriched top 30 GO terms. A. Total in SCC1 compared to LLC1. B. Upregulated in SCC2 compared to LLC1 cells. C. Downregulated in SCC2 compared to LLC1 cells in the GO enrichment analysis; the y-axis shows the log10-transformed *p*-value.

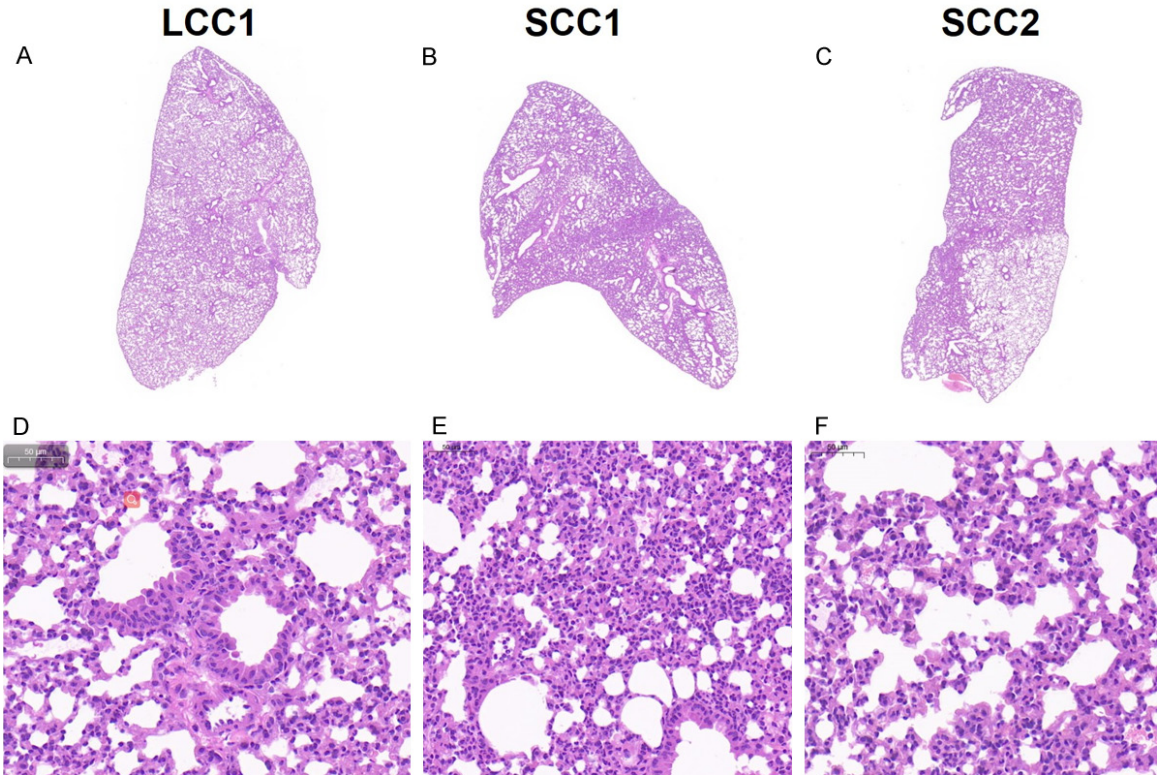

Supplementary Figure 6. Representative H&E stained lung sections in the three groups. A-C. The full scan images of lung slices of the three groups (1 ×). D-F. The representative lung in each group (20 ×).